CrossMark

Seasonal cycle of precipitation variability in South America on intraseasonal timescales

Carolina S. Vera[1,2] · Mariano S. Alvarez[1,2] · Paula L. M. Gonzalez[3,4] ·
Brant Liebmann[5,6] · George N. Kiladis[6]

Abstract The seasonal cycle of the intraseasonal (IS) variability of precipitation in South America is described through the analysis of bandpass filtered outgoing longwave radiation (OLR) anomalies. The analysis is discriminated between short (10–30 days) and long (30–90 days) intraseasonal timescales. The seasonal cycle of the 30–90-day IS variability can be well described by the activity of first leading pattern (EOF1) computed separately for the wet season (October–April) and the dry season (May–September). In agreement with previous works, the EOF1 spatial distribution during the wet season is that of a dipole with centers of actions in the South Atlantic Convergence Zone (SACZ) and southeastern South America (SESA), while during the dry season, only the last center is discernible. In both seasons, the pattern is highly influenced by the activity of the Madden–Julian Oscillation (MJO). Moreover, EOF1 is related with a tropical zonal-wavenumber-1 structure superposed with coherent wave trains extended along the South Pacific during the wet season, while during the dry season the wavenumber-1 structure is not observed. The 10–30-day IS variability of OLR in South America can be well represented by the activity of the EOF1 computed through considering all seasons together, a dipole but with the stronger center located over SESA. While the convection activity at the tropical band does not seem to influence its activity, there are evidences that the atmospheric variability at subtropical-extratropical regions might have a role. Subpolar wavetrains are observed in the Pacific throughout the year and less intense during DJF, while a path of wave energy dispersion along a subtropical wavetrain also characterizes the other seasons. Further work is needed to identify the sources of the 10–30-day-IS variability in South America.

✉ Mariano S. Alvarez
alvarez@cima.fcen.uba.ar

1 Departamento de Ciencias de la Atmósfera y los Océanos, Facultad de Ciencias Exactas y Naturales, Universidad de Buenos Aires, Buenos Aires, Argentina

2 Centro de Investigaciones del Mar y la Atmósfera (CIMA), Instituto Franco-Argentino del Clima y sus Impactos (UMI-IFAECI)/CNRS, CONICET-Universidad de Buenos Aires, Buenos Aires, Argentina

3 Department of Meteorology, University of Reading, Reading, UK

4 National Centre for Atmospheric Science, University of Reading, Reading, UK

5 CIRES, University of Colorado Boulder, Boulder, CO, USA

6 Physical Sciences Division, NOAA Earth System Research Laboratory, Boulder, CO, USA

1 Introduction

Climate variability in southern South America (SA) on intraseasonal timescales (IS) can exhibit large amplitude all year around (e.g. Gonzalez and Vera 2014; Alvarez et al. 2014). It is linked, to a large extent, to the large-scale circulation variability in both the tropics and extratropics, which in turn can be influenced by the Madden–Julian Oscillation (MJO; Madden and Julian 1994; Zhang 2005), by the activity of the Pacific South American (PSA) patterns (e.g. Li and Le Treut 1999) as well as in general by the dynamics of internal climate variability. MJO activity influencing SA has been identified all year round (Alvarez et al. 2016), as well as

that associated with the PSA patterns (Mo and Paegle 2001). Other IS phenomena affect SA, like blocking (Renwick 2005) and cut-off lows (Reboita et al. 2010), which are present in all seasons. Recently, Hirata and Grimm (2016a, b) described the interaction between synoptic and IS anomalies related to extreme rainfall events in SESA for all seasons.

It is well known that summer precipitation over SA exhibits significant variability on IS timescales (e.g. Gonzalez and Vera 2014 and references therein). The leading pattern, determined from filtered anomalies of outgoing longwave radiation (FOLR), is characterized by a dipole-like spatial structure with two centers of opposite signs located over southeastern SA (SESA) and the South Atlantic Convergence Zone (SACZ) regions, respectively (e.g. Casarin and Kousky 1986). Recently, Alvarez et al. (2014) showed that IS variability is also significant in SA during winter. The spatial structure of the leading pattern of the cold season FOLR, however, exhibits a monopole centered over SESA. Recently, Blázquez and Solman (2016) showed that monopole-like precipitation anomalies develop in that particular region on IS timescales in association with the corresponding variability of wintertime frontal activity. Moreover, during both summer and winter, the IS variability strongly modulates daily precipitation extremes (e.g. Liebmann et al. 2004; González et al. 2008; Alvarez et al. 2014) and surface temperature anomalies (including heat waves, Cerne and Vera 2011) in tropical and subtropical SA. The latter is not only relevant from a scientific point of view but also from a socio-economic perspective. Nevertheless, little progress has been made by the scientific community to describe and understand the seasonal variations of the IS variability in SA. To our knowledge, there are no previous studies describing and analyzing the leading patterns of IS variability in South America during the transition seasons, fall and spring.

The analysis of the leading patterns of IS variability throughout the year raises a question about what might be the best methodology to describe them. IS oscillations and related phenomena can span across seasons, and thus their analysis could be affected by the somewhat artificial season division that is traditionally used in this type of study. A better description and understanding of the seasonal cycle of the regional IS variability would be valuable for developing monitoring tools and subseasonal forecasts for week-2 and beyond.

The leading pattern of precipitation IS variability in SA exhibits large amplitudes at periods of around 20–25 days and at around 30–50 days during both, summer (e.g. Paegle et al. 2000) and winter (Alvarez et al. 2014). Recently, Gonzalez and Vera (2014) showed that the summer dipole activity in SA in the 30–90-day band is related to large-scale climate patterns like those associated with the MJO, while on the 10–30-day band the dynamics of tropical convergence zones and Rossby wavetrains could contribute to the

IS variability. Accordingly, Grimm and Dias (1995) showed, using a linear barotropic model, that the convection in the South Pacific Convergence Zone (SPCZ) is linked to the convective anomalies in SESA. However, to our knowledge, there are no previous studies analyzing the dynamics associated with the climate activity within both bands of IS variability during the other seasons. Considering that the mean and variability of the circulation in the SH and associated regional climate in SA, as well as the MJO, exhibit large seasonal variations, it is not a straightforward task to understand how the dynamics of both bands of IS variability behave throughout the year.

The objective of this study is thus to comprehensively describe the seasonal cycle of IS variability in SA and its relationship with both SH circulation anomalies and tropical convection. The study is based on the analysis of the activity of the leading pattern of FOLR in SA in two specific bands, 30–90 and 10–30 days. The paper is organized as follows: datasets and methodology are described in Sect. 2 with emphasis on discussing the approaches to describe the leading patterns of FOLR across seasons. They dynamics associated with the leading patterns of FOLR and their relation to tropical OLR, upper circulation and wave energy are described for each season in Sects. 3.1 and 3.2 for long (30–90 days) and short (10–30 days) IS timescales respectively, and a summary and conclusions are given in Sect. 4.

2 Data and methodology

Daily OLR data were obtained from the National Oceanic and Atmospheric Administration (NOAA) gridded dataset (Liebmann and Smith 1996). Daily means for 0.21-σ-level streamfunction were taken from the National Centers for Environmental Prediction-National Center for Atmospheric Research (NCEP-NCAR) reanalysis dataset (Kalnay et al. 1996). The 0.21-σ-level corresponds to roughly the upper tropospheric 200 hPa pressure surface. The period of study starts on October 1979 and ends on December 2013.

Daily anomalies of OLR and streamfunction were computed at every grid point by subtracting the seasonal cycle, defined as the 31-point smoothed series of climatological daily means. For the streamfunction anomalies, the zonal mean was also subtracted. Filtered OLR anomalies were obtained from a Lanczos-derived (Duchon 1979) cosine-weighted Fast-Fourier-Transform-based filter with 101 weights, and will be hereafter called as FOLR 10–30 and FOLR 30–90, respectively. Previous work (e.g. González et al. 2008) has confirmed that FOLR is a good indicator of IS variability of precipitation over SA.

EOF analysis based on the covariance matrix was applied to FOLR 10–30 and 30–90 to isolate the dominant pattern of variability (EOF1) on each band over the region 40°S–5°N

and 75°W–32.5°W, following Gonzalez and Vera (2014). The time series of the standardized first principal component (PC1) was considered as an EOF1 activity index and used to perform lagged linear regression maps of daily OLR and streamfunction anomalies. Based on the regressed streamfunction anomalies the horizontal components of the wave activity flux (WAF, Schubert and Park (1991)) were also computed to study Rossby wave propagation associated with the EOF patterns (Gonzalez and Vera 2014).

Regressed values were scaled to a value of one standard deviation of the corresponding PC1 and computed with 1-day lagged increment. The statistical significance of the local linear relationship between the PC1s and the dependent variable was assessed through a student's t test of the correlation coefficients. To account for the serial autocorrelation of the local correlation values, the sample size was corrected to the effective sample size following Wilks (2011). The regressed values are tested at a 95% confidence level.

3 Results

3.1 IS variability at 30–90 days

3.1.1 Leading patterns of regional variability

Various ways to represent the seasonal cycle of the IS variability of FOLR in the 30–90-day band were considered. First, the year was divided into four 3-month seasons: December–February (DJF), March–May (MAM), June–August (JJA) and September–November (SON). However, a strong resemblance was found between the leading patterns associated with the warmer seasons (SON, DJF and MAM, Fig. 1a–c). Previous studies have shown that the rainy season in the region of study, particularly centered on and to the east of Brazil and Paraguay, starts on average near the first or second fortnight of October, and it continues until April (e.g., Liebmann and Mechoso 2011). Furthermore, the SACZ is present in the rainy season, but not during the dry season (e.g. Vera et al. 2006). Previous studies have defined a warm or wet season as the period of 151 days centered on DJF (Gonzalez and Vera 2014; González et al. 2008) and a cold season as the 151-day period centered on JJA (Alvarez et al. 2014). Therefore, the year was also divided in two unequal seasons, from October to April (of length 212 days), defined as the wet season, and from May to September (of length 153 days), defined as the dry season.

The spatial distribution of the EOF1s obtained from FOLR 30-90 for the wet and dry seasons is displayed in Fig. 1e–f respectively. For comparison, Fig. 1a–d show the leading patterns obtained separately for SON, DJF, MAM and JJA respectively. During the wet season, when the SACZ is active, the EOF1 is a dipole with centers of action over the SACZ and SESA regions, though when the SACZ is not climatologically present, that is, in the dry season, EOF1 is characterized by a monopole located southward of the SACZ climatological position. The leading patterns obtained separately for each 3-month season show evidence of the dipole in SON, DJF and MAM (Fig. 1a–c). There are some slight differences mostly in the tilting of the positive center, but otherwise these patterns are very similar. On the other hand, the JJA pattern (Fig. 1d) resembles that of the dry season (Fig. 1f).

To quantify the similarity between the EOF1s, the spatial correlation between each of the spatial patterns was computed and is presented in Table 1. There is no spatial correlation between the wet and dry season patterns, which confirms that the precipitation in each season is modulated by a different IS mode of variability. Moreover, the correlation between EOF1 of the wet season and those of SON, DJF and MAM is large, and supports combining them into a single season while leaving the JJA season out because of lack of similarity (Table 1). The option of describing the seasonal cycle of the IS variability by computing a single EOF for the full year, to afterwards study its PC1 variability, was also considered (not shown). This option was proven to be unrealistic, as the resulting EOF1 (denoted in Table 1 as All year) is highly correlated with the pattern for the wet season but not with the dry season.

The variances explained by the leading patterns of the wet and dry seasons and by the four 3-month seasons are represented in Fig. 1g, including uncertainty bars defined following the North et al. (1982) criteria. EOF1 for the wet season explains 21.5% of the IS variance, similar to that explained by the DJF pattern, and slightly lower (higher) than that explained by the SON (MAM) patterns. On the other hand, EOF1 for the dry season explains 21.8%, which is lower than the variance explained when using only the JJA season. In every case, the non-overlapping uncertainty bars between EOF1 and EOF2 confirm that they are not degenerate (Fig. 1g).

3.1.2 Dynamics

Lagged regression maps were computed for OLR anomalies based on the PC1s and are presented in Fig. 2. As it was discussed before, the activity of the leading pattern of variability at 30-90 days of the wet season can be described with a single EOF. Nevertheless, in order to analyze the main dynamical features associated particularly with the onset, mature phase and demise of the wet season, three subseasons are considered: October–November (ON), December–January–February (DJF) and March–April (MA). Hereafter, the positive (negative) phase of EOF1 refers to when convection is enhanced (suppressed) in SESA. Accordingly,

Fig. 1 First EOF of FOLR 30–90 for **a** SON, **b** DJF, **c** MAM, **d** JJA, **e** wet season, **f** dry season. The domain in **a–d** is the same as in **e–f**. **g** Explained variance by the first three EOFS for each of the seasons, error bars follow the criteria of North
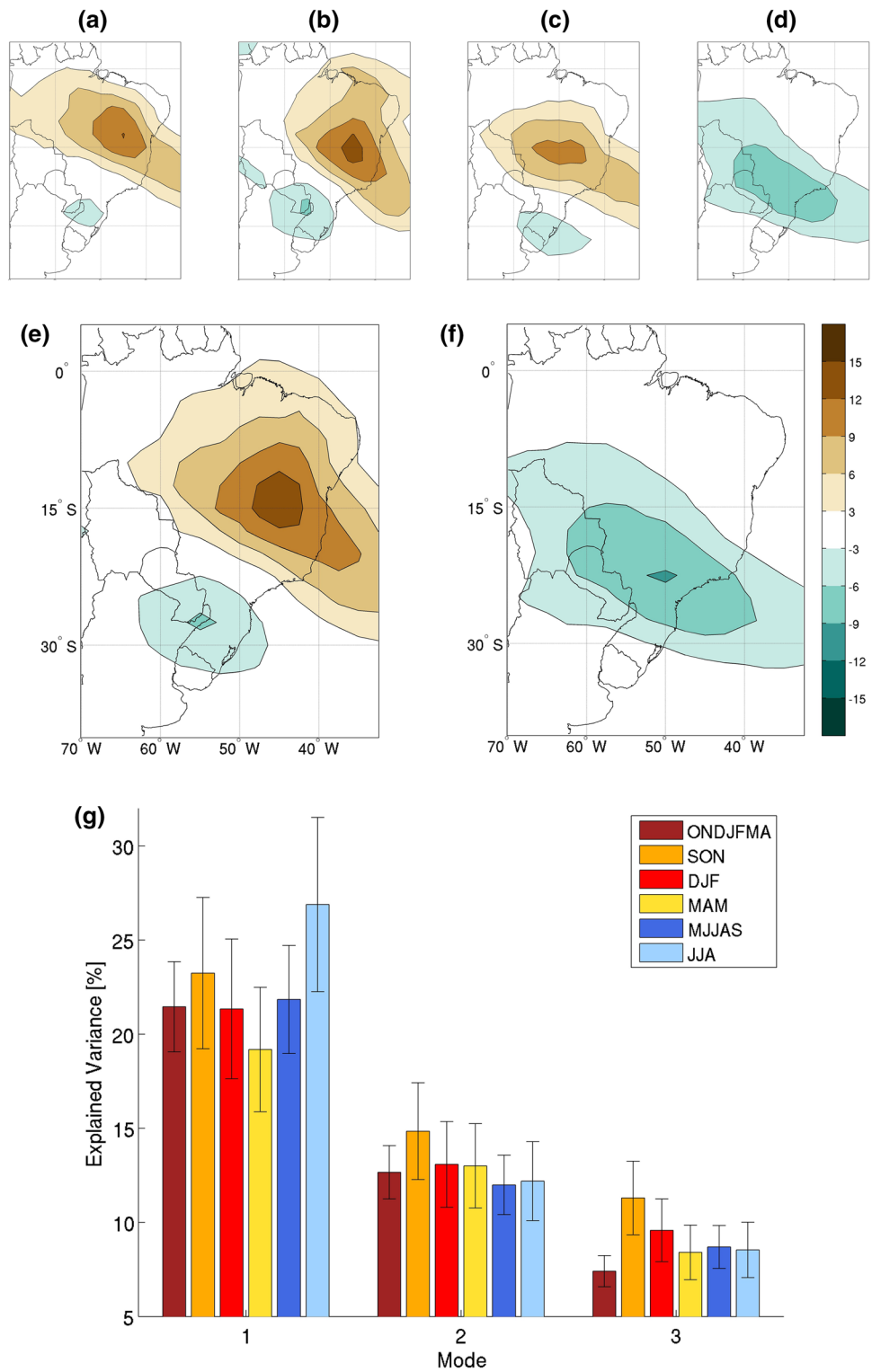
only those lags associated with the negative phases, the change of phase and positive phases (day 0 by construction) are shown in Fig. 2. The full evolution of the OLR anomaly lagged regression from day − 30 to day 0 is shown in an animation (Online Resource 1, O.r. 1), along with the

local evolution of the regressed OLR anomalies within each (the) center of action of the 30–90 FOLR EOF1 during the wet (dry) season.

In all three wet sub-seasons, OLR anomalies associated with the leading principal component are not confined

Table 1 Spatial correlation between the EOF1 of FOLR 30-90 according to season

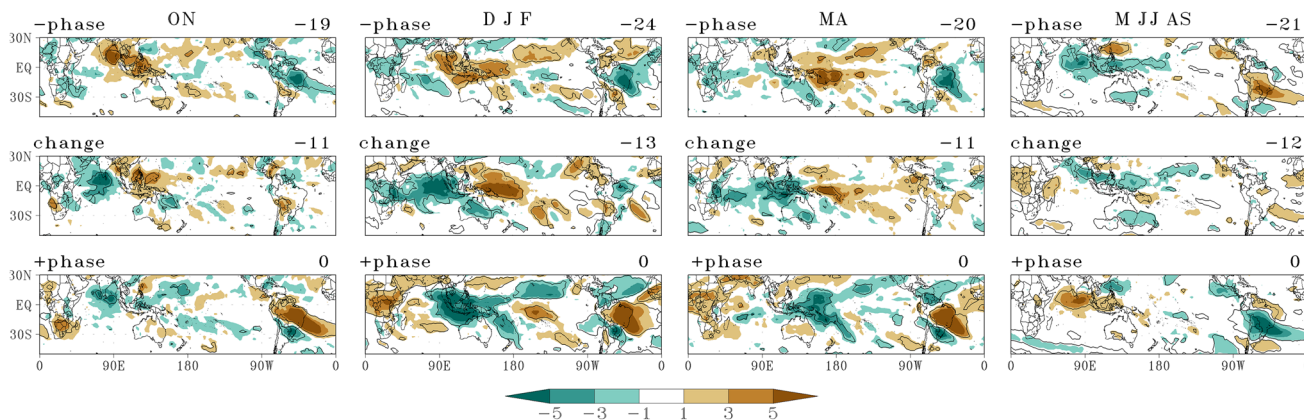| Season	All year	Wet	Dry	SON	DJF	MAM	JJA
All year	1	0.96	− 0.21	0.86	0.92	0.92	− 0.23
Wet	0.96	1	0.00	0.90	0.97	0.82	− 0.04
Dry	− 0.21	0.00	1	0.13	− 0.03	− 0.49	0.98
SON	0.86	0.90	0.13	1	0.78	0.69	0.06
DJF	0.92	0.97	− 0.03	0.78	1	0.77	− 0.05
MAM	0.92	0.82	− 0.49	0.69	0.77	1	− 0.51
JJA	− 0.23	− 0.04	0.98	0.06	− 0.05	− 0.51	1

Fig. 2 Maps of linear lagged regressions between OLR anomalies and the standardized PC1 30–90 for each season, for those lags in which the leading pattern of FOLR 30–90 showed the most intense negative phase, a change of phase and the most intense positive phase. First three columns correspond to the wet season, divided in ON, DJF and MA. The fourth column corresponds to the dry season. The values enclosed by the thick black contour are significant. Units in Wm^{-2}

locally to South America, but are also over the Indian and Pacific Oceans (Fig. 2). A comparison of the regressed values obtained for the positive phase (day 0) of the different sub-periods within the wet season, shows that the dipole in South America is dominant, as expected. However, in ON and MA the center associated with the SACZ is overall more zonally oriented than in DJF (Fig. 2), when it exhibits a more NW–SE orientation, typical of the mature state of the South American Monsoon System (e.g., Vera et al. 2006). Also, the dipole centers are more intense during DJF throughout the evolution of the activity of the leading pattern in South America (O.r. 1).

During ON, the anomalies are tropically-constrained, especially over the Indian Ocean and the western Maritime Continent, and move slowly from west to east (Fig. 2, O.r. 1). Positive OLR anomalies progress along the equator of the Indian Ocean starting on day − 30 and reach the Maritime Continent on day − 18 (O.r. 1). The evolution of this positive anomaly center between day − 30 and − 18 resembles that associated with the MJO average progression observed during austral spring between its phases 7 and 1 (Fig. 4 of Alvarez et al. (2016)), according with the Real-time Multivariate MJO (RMM) index (Wheeler and Hendon 2004).

Around day − 18, a negative center develops over the Indian Ocean, which then intensifies and moves to the east (Fig. 2, O.r. 1). Regionally, on around day − 20 (day 0) the negative (positive) anomaly over SACZ exhibits its largest magnitude, revealing a mean period of about 40 days associated with the dipole activity.

During DJF, the OLR anomalies in the Indian Ocean and the Maritime Continent are larger than in ON. During the negative EOF1 phase, a negative OLR anomaly center moves from Africa and the western Indian Ocean to the Maritime Continent and western Pacific Ocean on day 0 (Fig. 2, O.r. 1), when is straddled by two positive centers to the east and west. The evolution of these OLR anomalies from day − 30 to day 0 resembles the average MJO progression during austral summer between RMM phases 1 and 5 (Wheeler and Hendon 2004; Alvarez et al. 2016). Regionally, the dipole achieves a maximum negative phase on day − 24, and a maximum positive phase on day 0, yielding a 50-day period. In agreement, Alvarez et al. (2016) showed that the probability of enhanced precipitation is large (small) over the SACZ in MJO phase 1 (5), with the opposite behavior observed over SESA. The evolution of the tropical convective anomalies during MA is somewhat similar to DJF, although the

anomalies are slightly ahead in phase and weaker, with the positive center over the Pacific Ocean losing intensity and significance starting on day − 7 (Fig. 2, O.r. 1). Comparing the location of OLR anomalies between day − 12 and 0 to the evolution of the tropical divergent circulation during austral autumn from Alvarez et al. (2016), those days correspond to the RMM phases 3, 4 and 5 of the MJO. During MA, the dipole in South America exhibits a period of about 42 days.

During MJJAS, the dry season, a positive center of OLR regressed anomalies is located over SESA on day − 21, when convection is enhanced over the tropical Indian Ocean. During the next few days, the tropical convective center is displaced along tropical latitudes to the east, weakening considerably on day − 12, when a positive center of OLR anomalies starts to develop over the western Indian Ocean (Fig. 2, O.r. 1). The tropical anomaly pattern resembles that associated on average with MJO phases 6–8 (Fig. 3 of Alvarez et al. (2016)). On day 0, the center of suppressed convection reaches the Indian Ocean and a vast center of enhanced convection is observed over central South America (Fig. 2, O.r. 1). During the dry season, the monopole over South America exhibits a period of about 42 days.

The regression maps between 0.21-σ streamfunction anomalies and the PC1s were computed in the same manner as for the OLR and are displayed in Fig. 3, which also presents the WAFs derived from the regressed streamfunction anomalies. The full evolution of the streamfunction anomalies and WAFs since day − 30, along with the local evolution of the OLR regression within each (the) center of action of the EOF1 during the wet (dry) season is presented in Online

Resource 2 (O.r. 2). In agreement with Gonzalez and Vera (2014), the most prominent circulation features during the wet season are a zonal wavenumber-1 structure propagating eastward along the tropics and quasi-stationary circulation anomalies resembling Rossby wavetrains extended towards the extratropics. However, some differences within this season are noticeable. During ON, a strong quasi-stationary anticyclonic anomaly is located west of the Antarctic Peninsula before rainfall is favored in SESA starting on day − 19 (Fig. 3, O.r. 2). This feature is not observed in the other sub-seasons of the wet season, and agrees with the result of Solman and Orlanski (2010), who identified this pattern as a preconditioning condition for precipitation over the SESA. Also, during ON, the subpolar wavetrain along the South Pacific Ocean shows the lowest wavenumber signal of any season, and accordingly refracts to the northeast further to the south. The wave energy dispersion towards South America is mostly through subtropical latitudes from day − 30 until day − 11, since when the WAFs grow more intense along the subpolar wavetrain of the South Pacific Ocean (Fig. 3, O.r. 2).

During DJF, the energy disperses along the subpolar wavetrain observed in the negative (positive) phase of the South American dipole, when an anticyclonic (cyclonic) anomaly develops over southern South America favoring subsidence (ascending) conditions over SESA (Fig. 3, O.r. 2). During MA, from the negative to the positive phase of the dipole of OLR anomalies in South America, the subpolar wavetrain develops only 5 days before day 0, whereas during DJF and ON it does so starting on day − 13 (Fig. 3, O.r. 2).
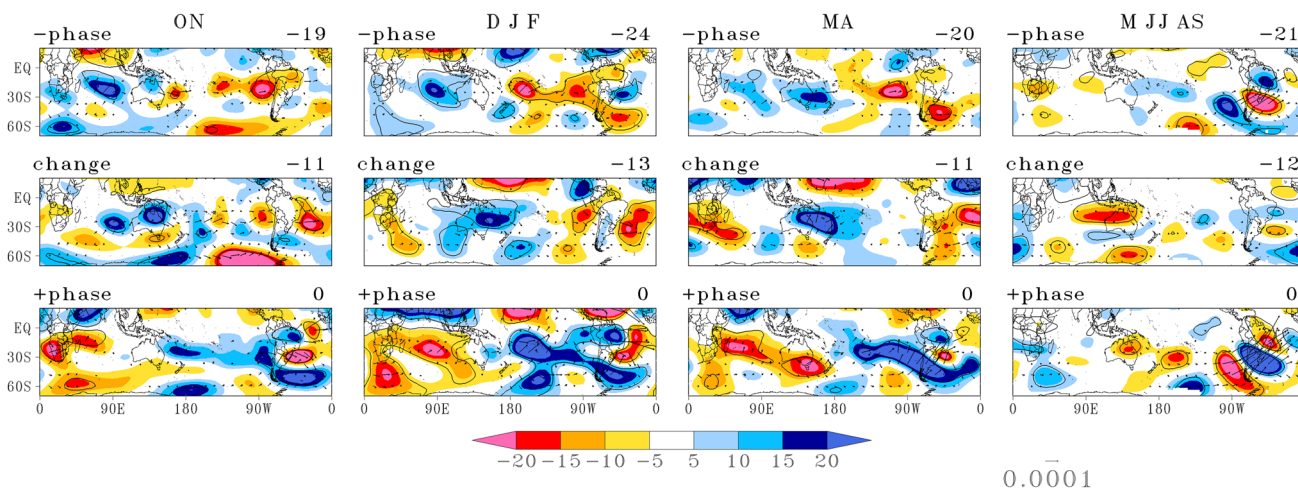

Fig. 3 Maps of linear lagged regressions between 0.21 σ-level streamfunction anomalies and the standardized PC1 30–90 for each season, for those lags in which the leading pattern of FOLR 30–90 showed the most intense negative phase, a change of phase and the most intense positive phase. First three columns correspond to the wet season, divided in ON, DJF and MA. The fourth column corresponds to the dry season. The values enclosed by the thick black contour are significant. Units in $10^{-5} m^2 s^{-1}$. Vectors represent the linear lagged regression of the wave activity fluxes for the 0.21 σ-level. The reference magnitude is shown in the bottom right and its units are $m^2 s^{-2}$

Furthermore, its wavenumber appears to be shorter than that of the DJF wavetrain, but not as short as during ON.

During MJJAS, the wavenumber-1 structure is not clear within the tropics (Fig. 3, O.r. 2), but a Rossby wave train arching along subpolar latitudes of the Pacific Ocean is observed. The teleconnection links to the anticyclonic (cyclonic) anomaly observed over central and northern Argentina during the negative (positive) phase of the EOF1 in South America. Also, starting on day − 9, circulation anomalies develop over the South Pacific Ocean, and the WAFs reveal that energy is propagated through both subtropical and subpolar latitudes, to converge in the negative center located in the eastern Pacific (Fig. 3, O.r. 2). This convergence of the energy maintains the cyclonic anomaly that explains the location of the negative OLR anomaly observed in subtropical South America on day 0 in Fig. 2.

3.2 IS variability at 10–30 days

3.2.1 Leading patterns of regional variability

The seasonal cycle of the IS variability of FOLR in the 10–30-day band was analyzed by computing the EOF1s for the 4 standard seasons, SON, DJF, MAM, and JJA as well as the EOF1 when considering all seasons together. It was found that the latter (Fig. 4e) represents the seasonal cycle quite well. EOF1 computed in such a way represents a dipole with a larger and more intense center of action over SESA and another one to the north. The same spatial distribution is evident in the EOF1s computed separately for each standard season (Fig. 4a–d). Moreover, from March to November, and even in DJF, the SESA center location and intensity is quite similar. The SACZ center, however, presents larger seasonal differences, being more intense in DJF and absent during JJA.

The variance explained by the leading patterns for the whole year and the four 3-month seasons are represented in Fig. 4f, in a similar way to Fig. 1g. EOF1 for the whole year explains 15.5% of the IS variance, like the amount explained by the DJF and MAM patterns, and about 5% lower than that explained by the SON and JJA patterns. Also, the non-overlapping error bars between EOF1 and 2 show that the first and second patterns are not degenerate (Fig. 4f).

Table 2 shows the spatial correlation values between the patterns computed for each season. The patterns for each season, as well as those computed for both wet and dry seasons, bear a reasonable resemblance to the pattern computed for the whole year. Therefore, the latter pattern is selected to describe the seasonal cycle of IS variability on 10–30 days.

3.2.2 Dynamics

The maps of OLR anomalies regressed against the PC1 previously separated for SON, DJF, MAM and JJA, so as to analyze the main seasonal dynamical features, are presented in Fig. 5. As before, only those lags for which the OLR regression showed a maximum in SESA/minimum in the SACZ region (negative phase), a change of sign and a minimum in SESA (positive phase, on day 0 by construction) are shown. The full evolution of the OLR anomaly lagged regressions from day − 15 to day 0 is shown in an animation (O.r. 3), along with the local evolution of the regression within each center of action of the 10–30 day FOLR EOF1 for the entire year.

During all seasons, positive (negative) OLR anomalies are observed in subtropical South America during the negative (positive) phase of the EOF1, with an average period of around 16 days. On day 0, the dipole-like structure is very clear during DJF, when there is no accompanying signal in the Southeast Pacific (Fig. 5, O.r. 3). In contrast, the regional pattern is most intense and better organized during JJA, when alternating centers of OLR anomalies are also observed along the South Pacific, arcing from the date line into South America. During the transitions seasons of SON and MAM, those centers are also discernible and significant, and their displacement to the east is clearly observed in the online animation (O.r. 3). Furthermore, the local evolution of the OLR regressed anomalies in the SACZ region during JJA displays only small amplitudes (O.r. 3).

Figure 6 presents the regression maps of the large-scale upper-level circulation anomalies against the PC1 and the derived WAFs, separately for SON, DJF, MAM and JJA seasons. The full evolution of the streamfunction anomalies and WAFs since day − 15, along with the local evolution of the OLR regression within each center of action of the 10–30 FOLR EOF1 are presented in the Online Resource 4 (O.r. 4). During all seasons, a strong cyclonic anomaly is located over central Argentina during day 0 (Fig. 6, O.r. 4) when the most intense convection center is developed over SESA (Fig. 5). However, circulation anomalies during DJF are considerably weaker than those observed during the other seasons. The latter can explain the absence of a wave-like signal observed in the DJF OLR regressed anomalies within the South Pacific ocean (Fig. 5). The WAFs in DJF show energy dispersion along subpolar South Pacific since the EOF1 phase change (Fig. 6, O.r. 4), while not along subtropical latitudes, as was observed for the 30–90 day band (Fig. 3). In contrast, during JJA, the WAFs highlight two paths of wave energy dispersion that maintain well defined wavetrains along both subpolar and subtropical latitudes of the South Pacific (Fig. 6, O.r. 4). The latter is consistent with

Fig. 4 First EOF of FOLR 10–30 for **a** SON, **b**, DJF, **c** MAM, **d** JJA, **e** All year. The domain in **a**–**d** is the same as in **e**. **f** Explained variance by the first three EOFS for each of the seasons, error bars follow the criteria of North
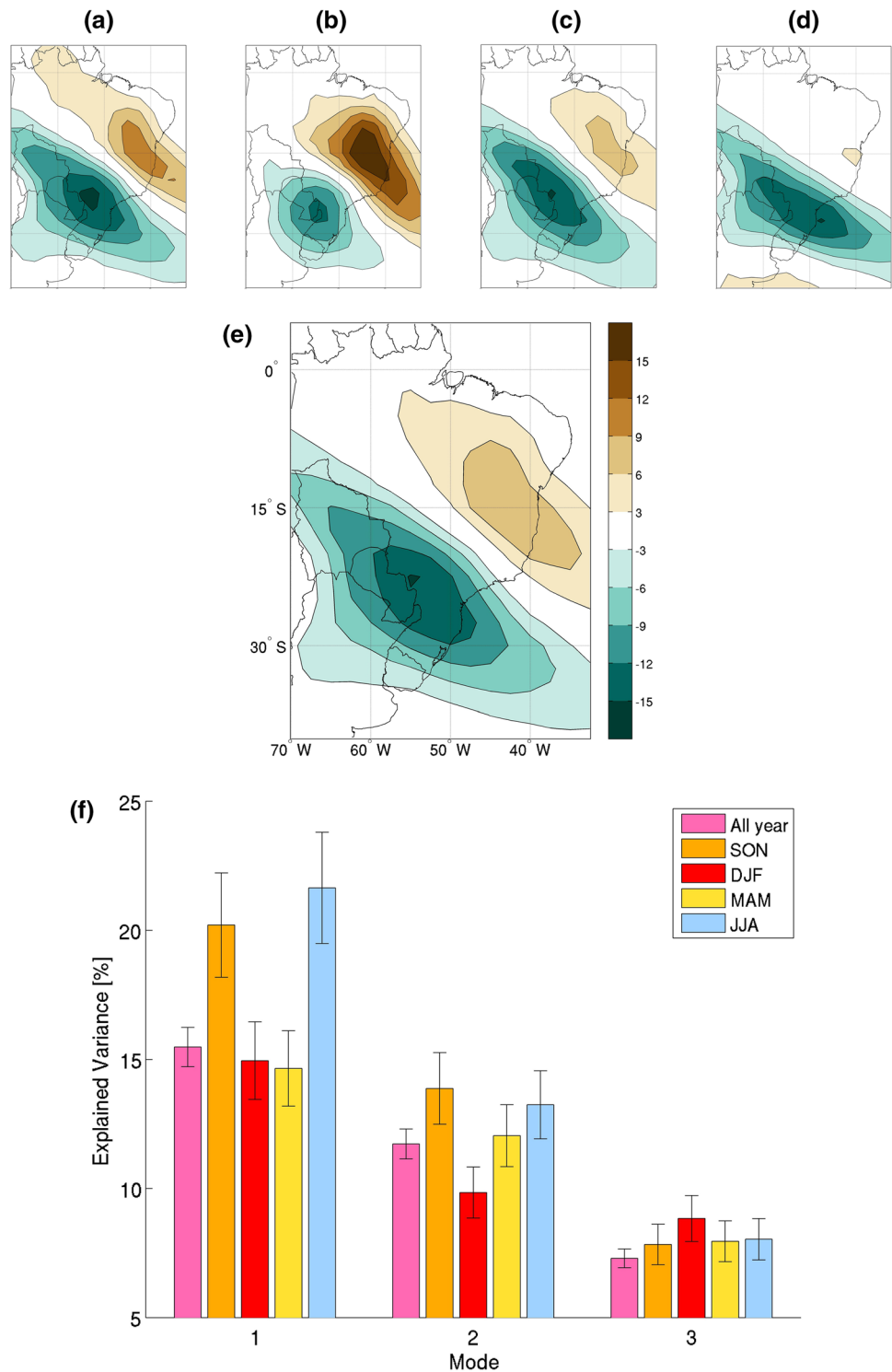
the double jet structure that characterizes the circulation of this season. In agreement, Alvarez et al. (2014) also showed the simultaneous activity of Rossby wavetrains along both

the subtropical and subpolar latitudes of the South Pacific in association with the evolution of the cold season 10–90-day FOLR EOF1 pattern in South America. However, this behavior was not found as significant in association with IS variability at 30–90 days (Fig. 3). Instead, the role of both jets in determining Rossby wave paths over the South Pacific was identified on synoptic scales (e.g. Vera et al.

Table 2 Spatial correlation between the EOF1 of FOLR 10–30 according to season

Season	All year	Wet	Dry	SON	DJF	MAM	JJA
All year	1	0.93	0.95	0.99	0.82	0.99	0.89
Wet	0.93	1	0.78	0.89	0.96	0.91	0.70
Dry	0.95	0.78	1	0.94	0.61	0.94	0.98
SON	0.99	0.89	0.94	1	0.76	0.97	0.88
DJF	0.82	0.96	0.61	0.76	1	0.79	0.54
MAM	0.99	0.91	0.94	0.97	0.79	1	0.54
JJA	0.89	0.70	0.98	0.88	0.54	0.87	1
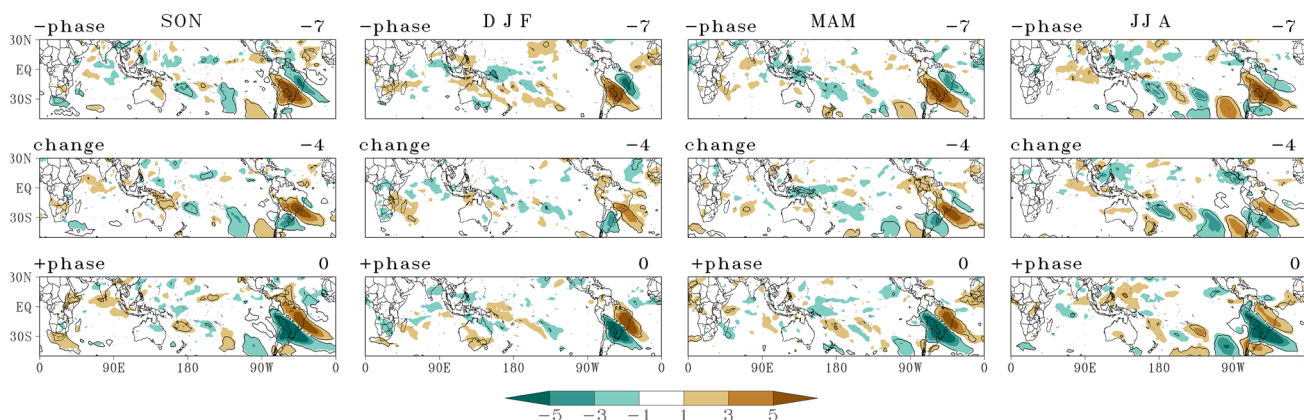
Fig. 5 Maps of linear lagged regressions between OLR anomalies and the standardized PC1 10–30 for each season, for those lags in which the leading pattern of FOLR 10–30 showed the most intense negative phase, a change of phase and the most intense positive phase. Each column corresponds to a trimester of the year. The values enclosed by the thick black contour are significant. Units in Wm^{-2}
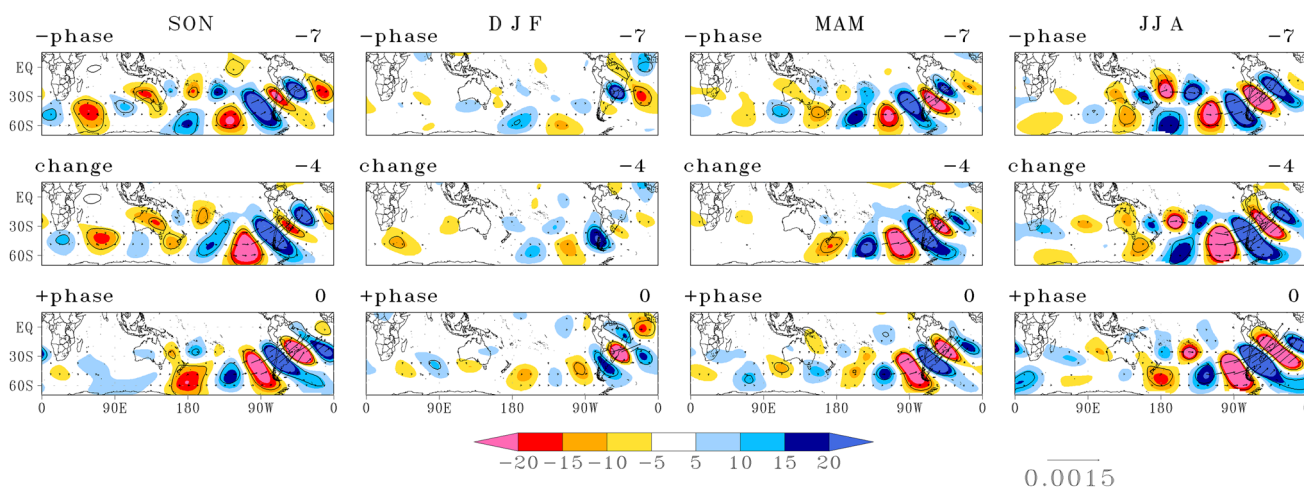

Fig. 6 Maps of linear lagged regressions between 0.21 σ-level streamfunction anomalies and the standardized PC1 10–30 for each season, for those lags in which the leading pattern of FOLR 10–30 showed the most intense negative phase, a change of phase and the most intense positive phase. Each column corresponds to a trimester of the year. The values enclosed by the thick black contour are significant. Units in 10^{-5}m^{2}s^{-1}. Vectors represent the linear lagged regression of the wave activity fluxes for the 0.21 σ-level. The reference magnitude is shown in the bottom right and its units are m^{2}s^{-2}

2002). Figure 6 also shows that both MAM and SON share features with those of JJA, such as the arcing energy pathways along subpolar latitudes of the Pacific Ocean and the splitting of the wavetrains, being clearer in SON than in MAM (Fig. 6, O.r. 4).

4 Summary and conclusions

In this paper, we provide a comprehensive description and dynamical analysis of the activity of the IS variability in SA spanning across seasons. Although such variability exhibits considerable amplitude all year long and it provides a strong modulation to the activity of daily extremes, the scientific community has so far focused most of its interest on that associated with the summer season only. Therefore, the study was intended to fill the knowledge gaps regarding the best approaches to describe the regional IS activity and the understanding of the main physical mechanisms explaining its behavior throughout the year.

We explore different ways to represent the seasonal cycle of the IS variability of FOLR in South America, in two specific bands, 30–90 and 10–30 days. For each IS band, the leading patterns were computed with an EOF analysis of the regional FOLR, and the associated dynamics was analyzed through computing regression maps between the corresponding PC1s and anomalies of different climate variables. The representation of the leading patterns of IS variability and the understanding of the associated large-scale mechanisms influencing it are important not only for theoretical reasons but also because such knowledge allows the development of better real-time monitoring and forecasting tools of regional IS variability.

Results show that the seasonal cycle of the 30–90-day IS variability in South America can be well described through the activity of the first EOF computed separately for the wet season (spanning from October to April) and the dry season (defined from May to September). The spatial distribution of wet-season EOF1 is that of a dipole, with a strong center of action in the SACZ region and a weaker one of opposite sign over SESA. The analysis of the evolution of the tropical convection anomalies associated with the activity of the regional pattern reveals that, in both wet and dry seasons, it is highly influenced by the activity of the MJO. Moreover, the analysis of the evolution of the upper-level streamfunction anomalies show that during the wet season there is an influence of a tropical zonal-wavenumber-1 structure like that induced by MJO. On the other hand, coherent wave trains extended along the South Pacific are also evident. However, seasonal differences are evident in the intensity, wavenumber and refraction latitude of the subpolar wavetrains, even within the wet season. The wavelengths seem to be shorter (longer) and circulation anomalies stronger

(weaker) during ON (DJF and MA). The fact that the MJO may be playing an important role on the activity of the leading pattern of long IS variability in South America provides good justification for future regional predictability studies.

The study also shows that the 10–30-day IS variability of OLR in South America could be well represented by the activity of the EOF1 computed through considering all seasons together. The spatial distribution of the leading pattern of 10–30-day IS variability is also a dipole, but with a stronger center over SESA and a weaker one of opposite sign within the SACZ region. The activity of this regional pattern which is characterized by a mean periodicity of around 16 days, a similar periodicity that was detected by Blázquez and Solman (2016), who associated frontal activity to the IS variability, particularly during the cold season. Even though the variability of the tropical convection over the Indian and Pacific Ocean does not seem to influence the activity of this regional pattern, this may be due to the linear regression technique used in this study. In fact, Raupp et al. (2008) and Raupp and Silva Dias (2010) discuss the possibility of nonlinear processes leading to internal variability on the IS scale through nonlinear resonance of equatorial waves, and associated this mechanism to convective forcing. The leading regional pattern is associated with the evolution of circulation anomalies organized in strong, arched subpolar wavetrains over the South Pacific Ocean. The associated wave energy dispersion maintains a strong circulation anomaly with NW–SE-tilt over subtropical South America, being cyclonic in association with enhanced convection in SESA. During JJA and SON, a strong subtropical wavetrain is also detected, being absent during DJF. It should be pointed out that the influence of the subtropical jet on the wavetrains was not that evident associated with the IS variability at 30–90 days. Therefore, the results obtained in this study confirm the need to better understand and simulate the interactions between the jets and the Rossby waves with periods shorter than 30 days. Nevertheless, future work needs to be done to better analyze sources of predictability associated with the 10–30-day IS variability in South America.

References

Alvarez MS, Vera CS, Kiladis GN, Liebmann B (2014) Intraseasonal variability in South America during the cold season. Clim Dyn 42(11):3253–3269. https://doi.org/10.1007/s00382-013-1872-z

Alvarez MS, Vera CS, Kiladis GN, Liebmann B (2016) Influence of the Madden Julian Oscillation on precipitation and surface air

temperature in South America. Clim Dyn 46(1):245–262. https://doi.org/10.1007/s00382-015-2581-6

Blázquez J, Solman SA (2016) Intraseasonal variability of wintertime frontal activity and its relationship with precipitation anomalies in the vicinity of South America. Clim Dyn 46(7):2327–2336. https://doi.org/10.1007/s00382-015-2704-0

Casarin D, Kousky V (1986) Precipitation anomalies in the southern part of brazil and variations of the atmospheric circulation. Rev Bras Meteor 1:83–90

Cerne SB, Vera CS (2011) Influence of the intraseasonal variability on heat waves in subtropical South America. Clim Dyn 36(11):2265–2277. https://doi.org/10.1007/s00382-010-0812-4

Duchon CE (1979) Lanczos filtering in one and two dimensions. J Appl Meteorol 18(8):1016–1022. https://doi.org/10.1175/1520-0450(1979)018<1016:LFIOAT>2.0.CO;2

Gonzalez PLM, Vera CS (2014) Summer precipitation variability over South America on long and short intraseasonal timescales. Clim Dyn 43(7):1993–2007. https://doi.org/10.1007/s00382-013-2023-2

González PLM, Vera CS, Liebmann B, Kiladis G (2008) Intraseasonal variability in subtropical South America as depicted by precipitation data. Clim Dyn 30(7):727–744. https://doi.org/10.1007/s00382-007-0319-9

Grimm AM, Dias PLS (1995) Analysis of tropical-extratropical interactions with influence functions of a barotropic model. J Atmos Sci 52(20):3538–3555. https://doi.org/10.1175/1520-0469(1995)052<3538:AOTIWI>2.0.CO;2

Hirata FE, Grimm AM (2016) The role of synoptic and intraseasonal anomalies in the life cycle of summer rainfall extremes over South America. Clim Dyn 46(9):3041–3055. https://doi.org/10.1007/s00382-015-2751-6

Hirata FE, Grimm AM (2016) The role of synoptic and intraseasonal anomalies on the life cycle of rainfall extremes over South America: non-summer conditions. Clim Dyn. https://doi.org/10.1007/s00382-016-3344-8.

Kalnay E, Kanamitsu M, Kistler R, Collins W, Deaven D, Gandin L, Iredell M, Saha S, White G, Woollen J, Zhu Y, Leetmaa A, Reynolds R, Chelliah M, Ebisuzaki W, Higgins W, Janowiak J, Mo KC, Ropelewski C, Wang J, Jenne R, Joseph D (1996) The ncep/ncar 40-year reanalysis project. Bull Am Meteorol Soc 77(3):437–471. https://doi.org/10.1175/1520-0477(1996)077<0437:TNYRP>2.0.CO;2

Li ZX, Le Treut H (1999) Transient behavior of the meridional moisture transport across South America and its relation to atmospheric circulation patterns. Geophys Res Lett 26(10):1409–1412

Liebmann B, Mechoso CR (2011) The South American Monsoon System. The global monsoon system. In: Chang C-P, Ding Y, Lau N-C (eds) The global monsoon system: research and forecast, 2nd edn. World Scientific Publication Company, Singapore, pp 137–157

Liebmann B, Smith CA (1996) Description of a complete (interpolated) outgoing longwave radiation dataset. Bull Am Meteorol Soc 77:1275–1277

Liebmann B, Vera CS, Carvalho LMV, Camilloni IA, Hoerling MP, Allured D, Barros VR, Baez J, Bidegain M (2004) An observed trend in central South American precipitation. J Clim 17(22):4357–4367. https://doi.org/10.1175/3205.1

Madden RA, Julian PR (1994) Observations of the 40–50-day tropical oscillation: a review. Mon Weather Rev 122(5):814–837. https://doi.org/10.1175/1520-0493(1994)122<0814:OOTDTO>2.0.CO;2

Mo KC, Paegle JN (2001) The pacific-South American modes and their downstream effects. Int J Climatol 21(10):1211–1229

North G, Bell T, Cahalan R, Moeng F (1982) Sampling errors in the estimation of empirical orthogonal functions. Mon Weather Rev 110:699–706

Paegle JN, Byerle LA, Mo KC (2000) Intraseasonal modulation of South American summer precipitation. Mon Weather Rev 128(3):837–850. https://doi.org/10.1175/1520-0493(2000)128<0837:IMOSAS>2.0.CO;2

Raupp CFM, Dias PLS, Tabak EG, Milewski P (2008) Resonant wave interactions in the equatorial waveguide. J Atmos Sci 65(11):3398–3418. https://doi.org/10.1175/2008JAS2387.1

Raupp CFM, Silva Dias PL (2010) Interaction of equatorial waves through resonance with the diurnal cycle of tropical heating. Tellus A 62(5):706–718

Reboita MS, Nieto R, Gimeno L, da Rocha RP, Ambrizzi T, Garreaud R, Krüger LF (2010) Climatological features of cutoff low systems in the southern hemisphere. J Geophys Res Atmos 115:D17104

Renwick JA (2005) Persistent positive anomalies in the southern hemisphere circulation. Mon Weather Rev 133(4):977–988. https://doi.org/10.1175/MWR2900.1

Schubert S, Park CK (1991) Low-frequency intraseasonal tropical–extratropical interactions. J Atmos Sci 48:629–650

Solman SA, Orlanski I (2010) Subpolar high anomaly preconditioning precipitation over South America. J Atmos Sci 67(5):1526–1542. https://doi.org/10.1175/2009JAS3309.1

Vera C, Higgins W, Amador J, Ambrizzi T, Garreaud R, Gochis D, Gutzler D, Lettenmaier D, Marengo J, Mechoso CR, Nogues-Paegle J, Dias PLS, Zhang C (2006) Toward a unified view of the american monsoon systems. J Clim 19(20):4977–5000. https://doi.org/10.1175/JCLI3896.1

Vera CS, Vigliarolo PK, Berbery EH (2002) Cold season synoptic-scale waves over subtropical south america. Mon Weather Rev 130(3):684–699. https://doi.org/10.1175/1520-0493(2002)130<0684:CSSSWO>2.0.CO;2

Wheeler MC, Hendon HH (2004) An all-season real-time multivariate MJO index: development of an index for monitoring and prediction. Mon Weather Rev 132(8):1917–1932. https://doi.org/10.1175/1520-0493(2004)132<1917:AARMMI>2.0.CO;2

Wilks D (2011) Statistical methods in the atmospheric sciences. Academic Press, Oxford

Zhang C (2005) Madden–Julian Oscillation. Rev Geophys 43(2):RG2003